An improved prediction of residual stresses and distortion in additive manufacturing

T. Mukherjee [a], W. Zhang [b], T. DebRoy [a,*]

[a] Department of Materials Science and Engineering, The Pennsylvania State University, University Park, PA 16802, USA
[b] Department of Materials Science and Engineering, The Ohio State University, Columbus, OH 43221, USA

A B S T R A C T

In laser assisted additive manufacturing (AM) an accurate estimation of residual stresses and distortion is necessary to achieve dimensional accuracy and prevent premature fatigue failure, delamination and buckling of components. Since many process variables affect AM, experimental measurements of residual stresses and distortion are time consuming and expensive. Numerical thermo-mechanical models can be used for their estimation, but the quality of calculations depends critically on the accurate transient temperature field which affects both the residual stresses and distortion. In this study, a well-tested, three-dimensional, transient heat transfer and fluid flow model is used to accurately calculate transient temperature field for the residual stress and distortion modeling. The calculated residual stress distributions are compared with independent experimental results. It is shown that the residual stresses can be significantly minimized by reducing the layer thickness during AM. Inconel 718 components are found to be more susceptible to delamination than Ti-6Al-4V parts because they encounter higher residual stresses compared to their yield strength.

© 2016 Elsevier B.V. All rights reserved.

1. Introduction

The additive manufacturing (AM) process involves heating, melting and solidification of an alloy by a moving heat source such as a laser or an electron beam in a layer by layer manner [1,2]. As a result, different regions of the work piece experience repeated heating and cooling [2]. The spatially varied thermal cycles result in residual stresses and distortion in the additively manufactured components [3]. The residual stresses, whose magnitude can exceed the yield strength of the alloy, affect corrosion resistance, fracture toughness, crack growth behavior and fatigue performance [4–8]. Moreover, the residual stresses are associated with pronounced deformations especially for thin-walled features [9–13]. Because AM involves many process variables as is the case with fusion welding, experimental measurements of stresses and strains are expensive and time consuming [4,14]. Moreover, experimental measurements depend on the shape and size of the components, nature of the stresses measured, sample preparation and accuracy of X-ray or neutron diffraction [7,14]. A recourse is to undertake calculations of residual stresses and strains in all locations of the work piece [15]. These calculations are often done in two steps in sequence. First, the transient temperature field in the entire work piece is calculated. The computed temperature results are then used for the mechanical calculations. Such sequential calculations of temperatures and stresses make the computations tractable but the accuracy of the calculations depends critically on the quality of the transient temperature field and the thermo-physical property data of the alloy.

As the laser or electron beam energy impinges on the work piece surface, the powder melts quickly to form a molten pool. The highest temperature on the molten pool surface is attained directly below the heat source and the temperature decreases with distance away from this location [16,17]. Inside the molten pool, the liquid alloy recirculates rapidly at very high velocities driven by the spatial gradient of surface tension. The convective flow mixes the liquid metal in different regions and enhances the transport of heat within the molten pool. The circulation pattern strongly affects the temperature distribution in the liquid alloy, heating and cooling rates, solidification pattern, and subsequently the evolution of various solid phases that make up the final microstructure of the part [18,19].

Simulation of complex physical processes that affect the temperature field is computationally intensive, and many of the previous calculations of the temperature field involved various simplifications and assumptions to make the calculations tractable. These include several two-dimensional models [20,21], or an

Table 1
Thermo-physical properties of Ti-6Al-4V and IN 718 [30].

Properties	Ti-6Al-4V	IN 718
Liquidus temperature (K)	1928	1609
Solidus temperature (K)	1878	1533
Thermal conductivity (W/m K)	$1.57 + 1.6 \times 10^{-2}\,T - 1 \times 10^{-6}\,T^2$	$0.56 + 2.9 \times 10^{-2}\,T - 7 \times 10^{-6}\,T^2$
Specific heat (J/kg K)	$492.4 + 0.025\,T - 4.18 \times 10^{-6}\,T^2$	$360.24 + 0.026\,T - 4 \times 10^{-6}\,T^2$
Density (kg/m³)	4000	8100
Viscosity (kg/m s)	4×10^{-3}	5×10^{-3}
$d\gamma/dT$ (N/m K)	-0.37×10^{-3}	-0.26×10^{-3}

assumption that the entire deposit is heated and then cooled [22], or building a part by a single layer deposition [23]. In some instances, heat sources have been simplified as surface flux to achieve computational speed [3,23–25]. Another common difficulty is that the calculations ignore the convective heat transfer which is the main mechanism of heat transfer within the liquid, as discussed previously [16–19]. This simplification can lead to the use of inaccurate temperature field for thermo-mechanical calculations [26–28], and the computed residual stress and strain fields do not always agree well with the corresponding experimental data.

The errors in the transient temperature fields and heating and cooling rates resulting from heat conduction calculations that ignore the molten metal convection are well documented in the literature. Svensson et al. noted that "...the heat conduction equation has been found to be inadequate in representing experimental cooling curves" [29]. Manvatkar et al. [16] showed that by ignoring the effect of convection, the cooling rates in additive manufacturing were over-estimated by about twice of the correct values. Therefore, the temperature distribution calculated using heat conduction models without extensive experimental calibrations is not accurate, which in turn, can adversely affect the accuracy in calculations of residual stresses and distortion. What is needed and not currently available is a numerical model that calculates residual stress and strain fields from the transient temperature distribution considering convective heat transfer.

Here we combine a well-tested three-dimensional transient heat transfer and fluid flow model of additive manufacturing with a thermo-mechanical model to accurately calculate the temperature fields, residual stresses and distortion. The calculated temperature and residual stress distributions are tested using independent experimental results. After validation, the model is used to quantitatively study the effect of a wide variety of AM variables such as heat input and layer thickness on residual stresses and distortion. Although the results shown in this article are for direct energy deposition process, the findings will be useful to make dimensionally compliant components and assess residual stresses for all laser assisted powder based AM processes.

2. Modeling

2.1. Assumptions

Some simplified assumptions are made in both the heat transfer and fluid flow model and the thermo-mechanical model. The densities of the solid and liquid metals are assumed to be constant. The surfaces of the deposited layers are considered to be flat. The loss of alloying elements due to vaporization and its effects on both the heat loss and composition change are not incorporated in the present calculations. Finally, the effects of strains induced by solid-state phase transformation and creep are also neglected.

2.2. Governing equations

A well tested, three dimensional, transient, heat transfer and fluid flow model for AM [16,17] is used to compute temperature

and liquid metal velocity fields. The model solves the following equations of conservation of mass, momentum and energy [18,19] in three dimensions.

$$\frac{\partial(\rho u_i)}{\partial x_i} = 0 \tag{1}$$

$$\frac{\partial(\rho u_j)}{\partial t} + \frac{\partial(\rho u_j u_i)}{\partial x_i} = \frac{\partial}{\partial x_i}\left(\mu \frac{\partial u_j}{\partial x_i}\right) + S_j \tag{2}$$

where ρ is the density, u_i and u_j are the velocity components along the i and j directions, respectively, and x_i is the distance along the i direction, t is the time, μ is the effective viscosity, and S_j is a source term for the momentum equation. The energy conservation equation is:

$$\rho \frac{\partial h}{\partial t} + \frac{\partial(\rho u_i h)}{\partial x_i} = \frac{\partial}{\partial x_i}\left(\frac{k}{C_p}\frac{\partial h}{\partial x_i}\right) - \rho \frac{\partial \Delta H}{\partial t} - \rho \frac{\partial(u_i \Delta H)}{\partial x_i} \tag{3}$$

where h is the sensible heat, C_p is the specific heat, k is the thermal conductivity, and ΔH is the latent heat content. Table 1 shows the thermo-physical properties of the alloys used for the calculations.

The temperature field as a function of time calculated from the heat transfer and fluid flow model is then imported to a mechanical model based on Abaqus®, a commercial finite element analysis (FEA) code [31]. The total strain increment ($\Delta \varepsilon_{lm}^{tot}$) with respect to time is contributed by the several effects shown below:

$$\Delta \varepsilon_{lm}^{tot} = \Delta \varepsilon_{lm}^{E} + \Delta \varepsilon_{lm}^{P} + \Delta \varepsilon_{lm}^{Th} + \Delta \varepsilon_{lm}^{V} \tag{4}$$

where $\Delta \varepsilon_{lm}^{E}$, $\Delta \varepsilon_{lm}^{P}$ and $\Delta \varepsilon_{lm}^{Th}$ are the elastic, plastic and thermal strain increments respectively. $\Delta \varepsilon_{lm}^{V}$ is the strain induced due to the solid state phase transformation and creep, which is assumed to be zero in the present model. The resulting stress increment estimated from the elastic strain as [5]:

$$\Delta \sigma_{ij}^{E} = D_{ijlm} \cdot \Delta \varepsilon_{lm}^{E} \tag{5}$$

where D_{ijlm} is the elastic stiffness matrix calculated from Young's modulus (E) and Poisson's ratio (v) as,

$$D_{ijlm} = \frac{E}{1+v}\left[\frac{1}{2}(\delta_{ij}\delta_{lm} + \delta_{il}\delta_{jm}) + \frac{v}{1-2v}\delta_{ij}\delta_{lm}\right] \tag{6}$$

where δ is a Dirac delta function [32] whose value is one only for $i = j$ and $l = m$, and is zero otherwise. Temperature-dependent plasticity with the von Mises yield criterion [5] is utilized to model the flow stress and plastic strain. The thermal strain increment is calculated as:

$$\Delta \varepsilon_{lm}^{Th} = \beta \delta_{lm} \Delta T \tag{7}$$

where β is the volumetric thermal expansion coefficient and ΔT is the temperature increment. The temperature-dependent mechanical properties used for the calculations for Inconel 718 and Ti-6Al-4V are given in Tables 2 and 3, respectively. The step-by-step procedure for calculating temperature distribution, residual stresses and distortion is illustrated in Table 4. A Python script was developed to facilitate mapping the transient temperature fields from the heat transfer and fluid flow model to the Abaqus-based

Table 2
Temperature dependent mechanical properties of IN 718 [33].

Temperature (K)	Young's modulus (GPa)	Temperature (K)	Volumetric expansion co-efficient (/K)	Temperature (K)	Yield stress (MPa)
300	156.3	300	1.17E−05	300	308.9
366.5	151.8	477.6	1.28E−05	588.7	246.3
477.6	144.9	588.7	1.34E−05	810.9	226.1
588.7	138	922	1.46E−05	1033.2	207.7
699.8	131.4	1033.2	1.51E−05	1255.4	114
810.9	124.7	1144.3	1.57E−05		
922	124	1366.5	1.66E−05		
1033.2	123.4	1672	1.66E−05		
1144.3	107.7	1900	1.42E−05		
1255.4	92.05	2400	1.08E−05		
1366.5	68.95	2700	9.47E−06		
1672	23.79	3200	7.84E−06		

Table 3
Temperature dependent mechanical properties of Ti-6Al-4V [34,35].

Temperature (K)	Young's modulus (GPa)	Temperature (K)	Volumetric expansion co-efficient (/K)	Temperature (K)	Yield stress (MPa)
300	125	300	8.78E−06	300	955
533	110	533	9.83E−06	573	836
589	100	589	1.00E−05	773	732
700	93	700	1.07E−05	1023	581
755	80	755	1.11E−05	1073	547
811	74	811	1.12E−05	1173	480
923	55	923	1.17E−05	1273	405
1073	27	1073	1.22E−05	1373	330
1098	22	1098	1.23E−05		
1123	18	1123	1.24E−05		
1573	12	1573	1.30E−05		
1873	9	1873	1.63E−05		

Table 4
Outline of the sequentially-coupled model combining the heat transfer and fluid flow model with the FEA model.

| Computational model	Inputs	Outputs	Description
3D transient heat transfer and fluid flow model	Process parameters and temperature dependent thermo-physical properties of the alloys	Temperature and velocity fields	The model solves the equations of conservation of mass, momentum and energy in a 3D discretized solution domain consisted of the substrate, and deposited layers
Importing the nodes, elements and temperature data to the FEA model	Nodes, elements and temperature data from the heat transfer and fluid flow model	A temperature field data file (ODB) that can be imported in the FEA solver for mechanical analysis	A Python script that combines all nodes, elements and corresponding transient temperature data and generates an ODB file that can be directly used in the Abaqus-based FEA solver to calculate stress and strain fields
Abaqus-based FEA model for stress and strain calculations	Nodes, elements, boundary conditions, transient temperature data, and temperature-dependent mechanical properties of the alloys	Transient stress and strain fields	Finite element solution of static force equilibrium equations in the discretized solution domain for the temperature data calculated using the heat transfer and fluid flow model

FEA model. The script used the Abaqus Scripting Interface, an application programming interface (API), to create an ODB file that contained the transient temperature fields. Compared to the other option using Abaqus user subroutine UTEMP to load temperature fields into the stress model, the ODB file had the advantage of more easily handling large dataset of temperature fields.

2.3. Heat source model and boundary conditions

The volumetric heat source term for laser beam used in the heat transfer and fluid flow model is expressed by the following equation [16]:

$$S_i = \frac{Pd}{\pi r_b^2 \lambda} [\eta_P + (1 - \eta_P)\eta_l] \exp\left(-d\frac{r^2}{r_b^2}\right) \tag{8}$$

where η_P is the fraction of laser energy absorbed by the powder during flight from nozzle to substrate, η_l refers to the absorption coefficient of the deposited layer, P is the laser power, d is the laser
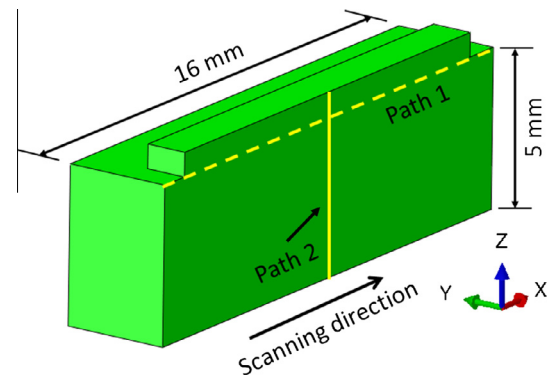

Fig. 1. Solution domain for the heat transfer and fluid flow and mechanical analysis. Due to the symmetry, a half of the solution domain is considered to reduce time and computer memory requirements for the analysis. The two path along which residual stress values are calculated are shown.

Table 5
Process parameters used for calculations.

Parameter set	Laser power (W)	Beam radius (mm)	Scanning speed (mm/s)	Layer thickness (mm)	Substrate thickness (mm)	Powder flow rate (g/s)
1	2000	1.5	10.5	0.90	10	0.432
2	600	0.8	4	0.67	11	0.358
3	200–400	0.5	15	0.4–0.8	4	0.416
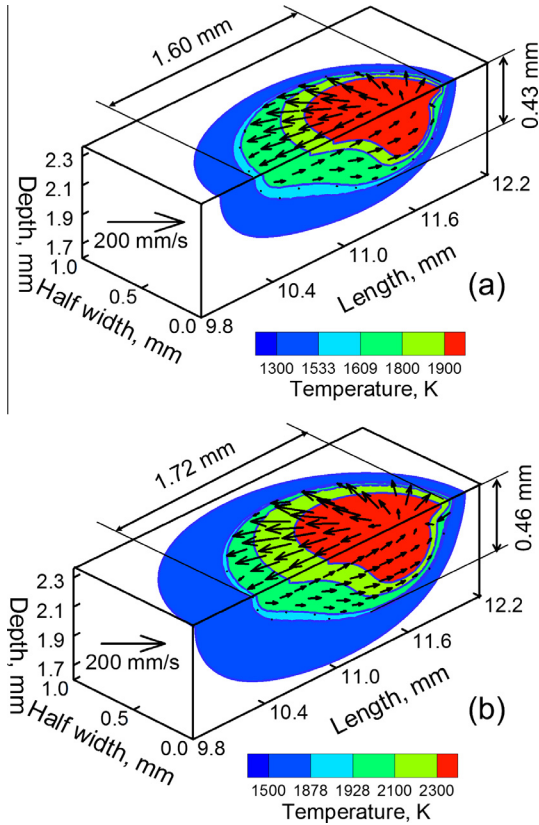
Fig. 2. Temperature and velocity distributions during the deposition of the 2nd layer for (a) IN 718 and (b) Ti-6Al-4V. The simulation is done for 250 W laser power, 15 mm/s scanning speed and 0.4 mm layer thickness.

Fig. 3. Temperature variation with time at different locations on the top surface for different y-values but at x = 4.5 mm. This temperature distribution is for a single layer laser assisted deposition of IN 718 powder on IN 718 substrate using the power of 250 W and 15 mm/s scanning speed.

beam intensity distribution factor, λ is the layer thickness, r_b is the focused beam radius and r is the radial distance from the beam axis. Other boundary conditions for the thermal analysis include heat loss by convection and radiation to the surroundings. The convective flow of molten metal inside the pool is driven by the surface tension gradient on the top surface of the pool resulting from the spatial variation of temperature [18,19]. The resulting Marangoni stress can be expressed as [19]:

$$\tau = \frac{d\gamma}{dT}\frac{dT}{dr} = \mu\frac{du}{dz} \qquad (9)$$

where T is the temperature, γ is the surface tension, τ is the Marangoni stress, and r is the radial distance from the axis of the heat source. Fig. 1 represents the solution domain of a 14-mm-long deposit on a 5-mm-thick and 16-mm-long substrate. Calculations are done over a half of the geometry taking advantage of symmetry. The laser beam travels along the positive x-axis. Positive z-axis represents the build direction vertically upward. The boundary conditions for the Abaqus-based mechanical analysis include fixed bottom surface, i.e., the displacements of all nodes of the bottom surface along the x, y and z directions are zero. Table 5 summarizes the additive manufacturing process parameters used in the calculations.

The stresses along x, y and z directions are referred to as the longitudinal, transverse and through-thickness stresses, respectively. From the calculated stress field, these individual residual stress components are extracted along paths 1 and the 2, as shown in Fig. 1. The longitudinal residual stress along path 1 is important because it is a driving force for crack propagation, buckling and distortion. The through-thickness stress along path 2 can be responsible for delamination [23–25].

3. Results and discussions

Fig. 2 shows the computed temperature and velocity fields, and the shape and size of molten pool for IN 718 and Ti-6Al-4V during deposition of the second layer. Each color[1] band in Fig. 2 represents a temperature range shown in the legend and the molten pool lengths are indicated in the figures. It shows that the molten pool size for Ti-6Al-4V is slightly larger than that for IN 718 for the same laser power and scanning speed mainly because of the lower density of Ti-6Al-4V as shown in Table 1. The computed velocity fields in Fig. 2 result from the spatial gradient of surface tension on the top surface of the molten pool. A reference vector is shown by an arrow and a comparison of the length of this arrow with the vectors in the plots indicates the magnitudes of the computed velocities. The results show a strong recirculatory flow of liquid metal from the middle of the pool to the periphery. For the processing conditions considered here, the values of Peclet numbers are significantly higher than 1 (between 9 and 13). Therefore, the calculated Peclet numbers and the magnitude of the velocities clearly show the dominance of convective heat transfer over heat transfer by conduction.

The temperature field in AM is highly transient as well as spatially non-uniform. Fig. 3 represents the temperature variation as a function of time for different locations along the deposit width (y-distance) starting from the pool center (y = 0) for IN 718 deposit.

---

[1] For interpretation of color in Fig. 2, the reader is referred to the web version of this article.
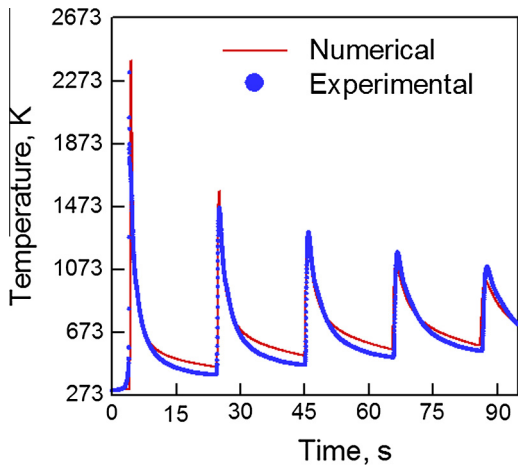
Fig. 4. Comparison of experimentally measured [36] and numerically computed thermal cycle for a 5 layers laser assisted deposition of 150 mm long Ti-6Al-4V deposit on Ti-6Al-4V substrate using process parameter set 1 in Table 5. The monitoring location is at the mid length of the deposit on the top surface of the substrate.

The peak temperature is the highest at the pool center and decreases gradually with distance away from the center. The variation of the temperature with respect to time represents the thermal cycle. Fig. 4 shows that the calculated thermal cycle agrees

well with the experimentally measured values [36] for a 5-layer-high deposition of a 150-mm-long Ti-6Al-4V build. The temperature was experimentally measured using a thermocouple located on the top of the substrate at the mid length of the deposit. Thermal cycles are simulated for the entire build using a corresponding solution domain of 150 mm length. The excellent agreement between the experimental and theoretical calculations shows the importance of considering both conduction and convection in the simulation. The agreement also indicates that the computed transient temperature field can be used for the residual stress and strain calculations with confidence.

Fig. 5 shows the temperature distribution for different layers during a 10-layer-high deposition of IN 718 powder. In AM, the substrate acts as a heat sink. Therefore, for the upper layers, heat transfer through the substrate decreases, which in turn, effectively increases the peak temperature for the upper layers. Because of the rapid scanning of laser beam the temperature contours are elongated behind the heat source and compressed in front of the beam. The highly transient and spatially non-uniform temperature distribution, such as that shown in Fig. 5, is responsible for the generation of the stress and strain fields.

Fig. 6 shows the evolution of the longitudinal strain field during the deposition of IN 718. With the progress of the deposition process, more heat accumulates in the work piece. Also, both the peak temperature and the pool volume increase slightly while at the same time the stiffness drops for the upper layers because of
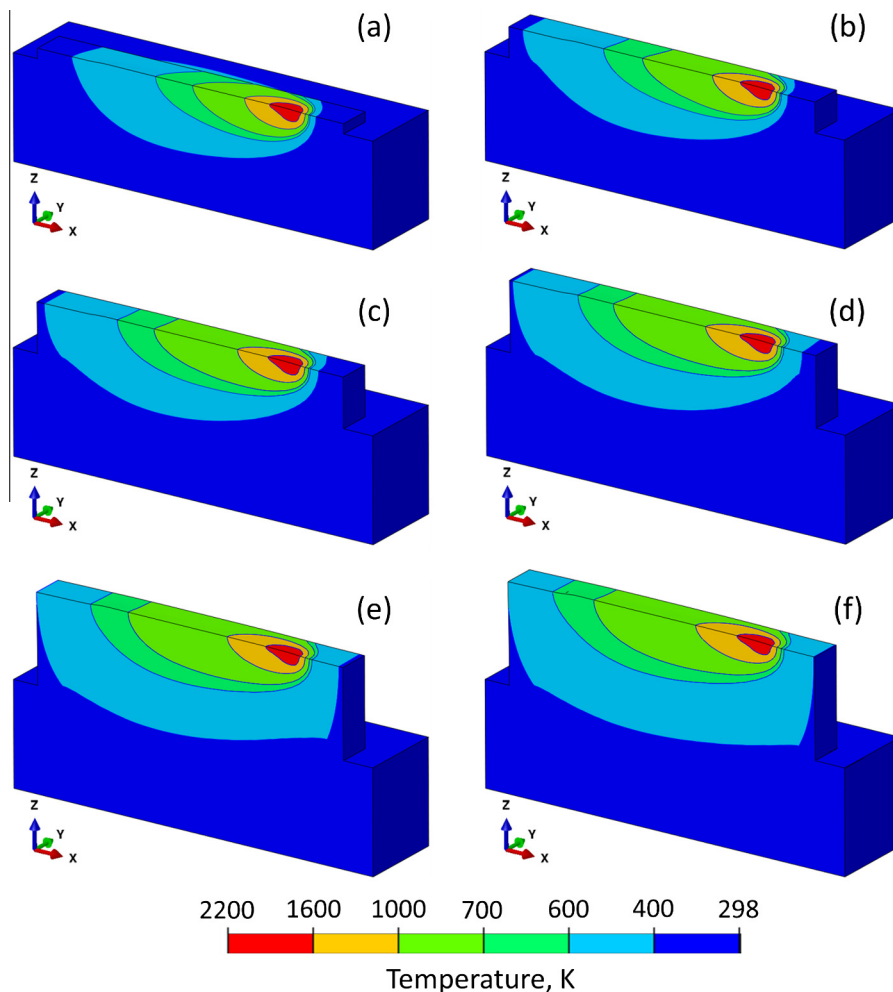
Fig. 5. Temperature distribution during the deposition of (a) 1st (b) 3rd (c) 5th (d) 7th (e) 9th and (f) 10th layer deposition of IN 718 powder on IN 718 substrate. The laser beam position is 10 mm from the starting point of the deposition. Laser beam scanning direction is along the positive x-axis. This simulation is done for 300 W laser power and 15 mm/s scanning speed for the solution domain in Fig. 1.
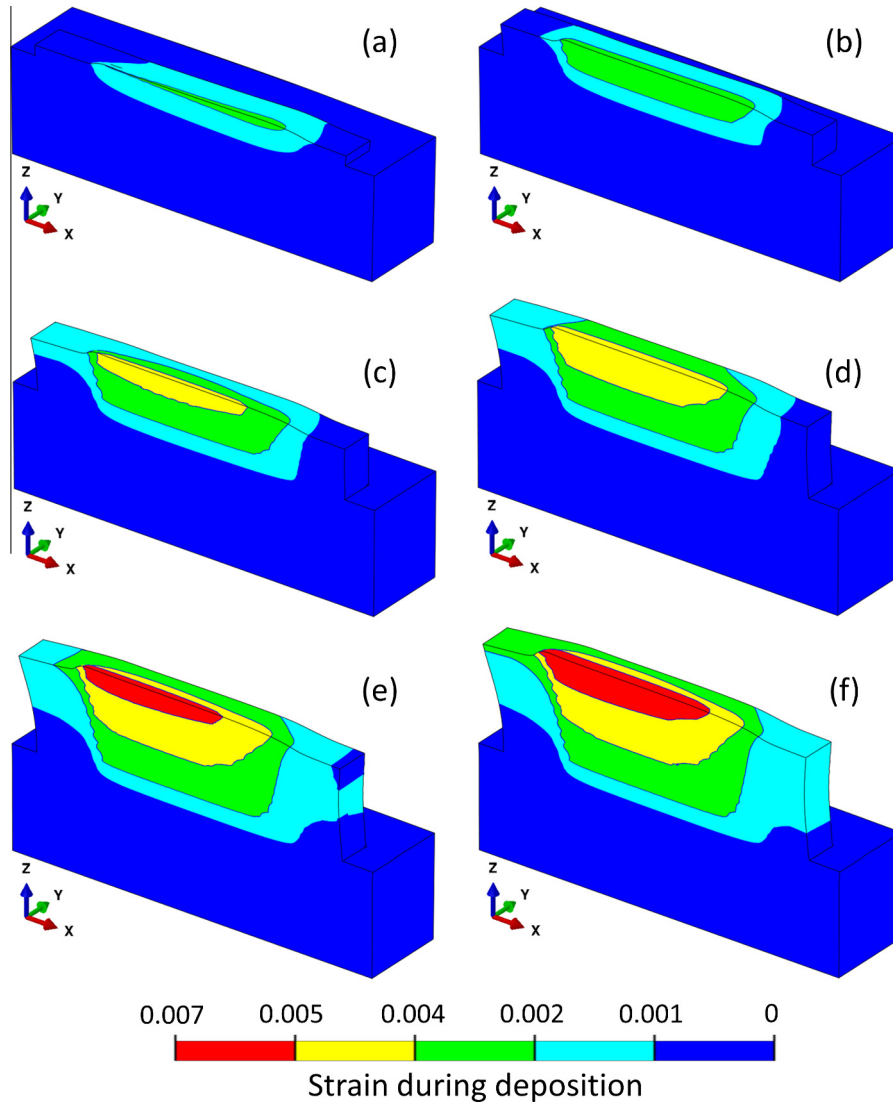
Fig. 6. Longitudinal strain field at the end of depositing (a) 1st (b) 3rd (c) 5th (d) 7th (e) 9th and (f) 10th layer deposition of IN 718 powder on IN 718 substrate. Laser beam scanning direction is along the positive x-axis. This simulation is done for 300 W laser power and 15 mm/s scanning speed for the solution domain in Fig. 1. Deformation is magnified by 10×.
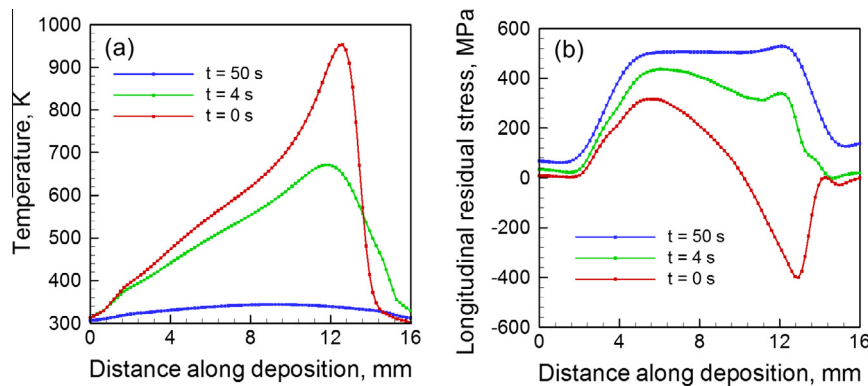
Fig. 7. Variation in (a) temperature distribution and (b) longitudinal stress distribution along path 1 with time after the laser beam extinguishes at the end of 2nd layer. This simulation is done for IN 718 powder deposited on IN 718 substrate with 300 W laser power and 15 mm/s scanning speed. "t" represents the time after the laser beam extinguishes at the end of the deposition.

higher temperatures. Therefore, the strain value increases continuously for the upper layers as shown in Fig. 6(a)–(f). The results indicate that thin-walled, taller structures are more susceptible to deformation than the shorter ones.

Evolution of the stresses depends on the transient temperature distribution especially during cooling of the deposit. Fig. 7(a) shows the temperature distribution along path 1 during cooling of the build. Fig. 7(b) represents the corresponding longitudinal
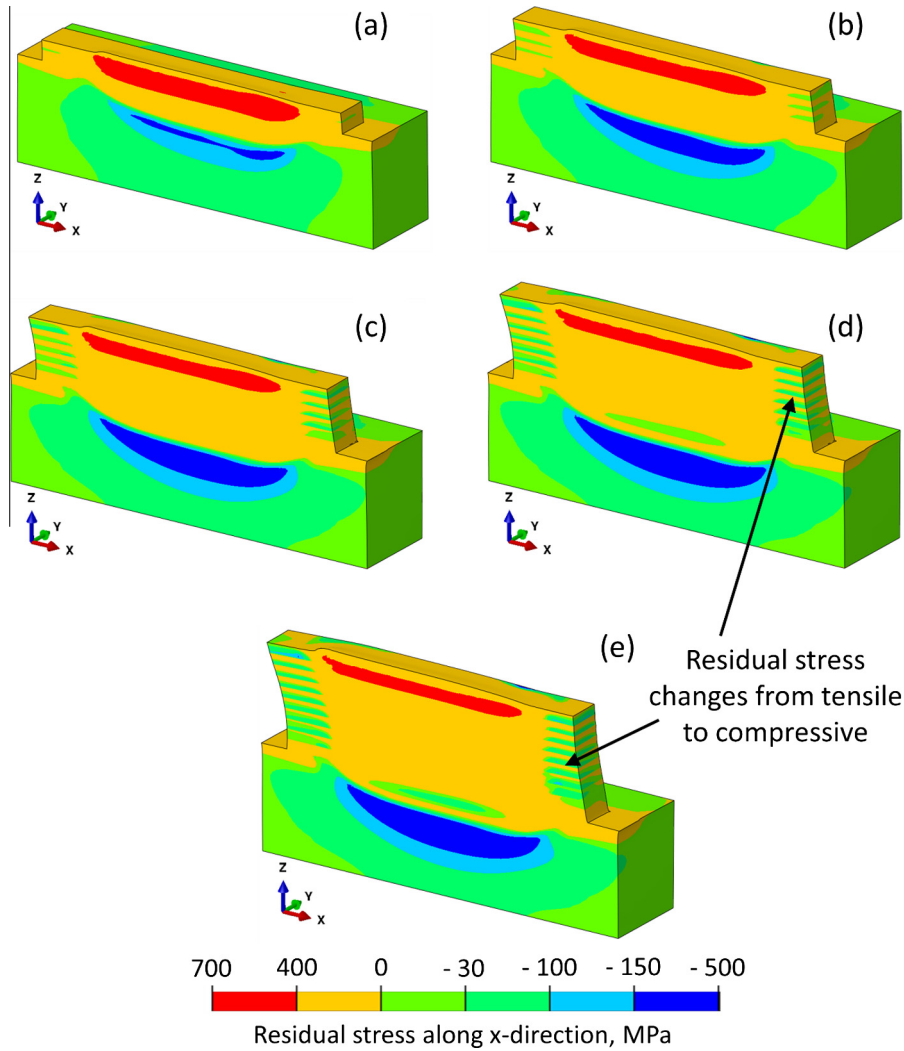
Fig. 8. Residual stress along x-direction (longitudinal) at the end of the deposition of (a) 2nd (b) 4th (c) 6th (d) 8th and (e) 10th layer of IN 718 powder on IN 718 substrate. Laser beam scanning direction is along the positive x-axis. This simulation is done for 300 W laser power and 15 mm/s scanning speed for the solution domain in Fig. 1. Deformation is magnified by 10×.

stress profile developed along path 1. At t = 0 s, i.e., just after the laser beam traverses the entire length and is switched off temporarily to prepare for the deposition of the next layer, the peak temperature of the deposit along path 1 (located at the substrate-deposit interface) is about 950 K. This high temperature softens the material locally. Therefore, the magnitude of the stress is relatively low as it is limited by the yield strength at the high temperature. The stress field evolves as the deposit continues to cool down further. After 50 s, the temperature of the deposit almost cools down to the room temperature and the longitudinal stress along path 1 is highly tensile, as shown in Fig. 7(b). If there was no additional layer deposited, the stress field at the end of cooling would not change further, thus corresponding to the residual stress field in the part.

Figs. 8–10 show the distribution of the residual stresses along x (longitudinal), y (transverse) and z (through-thickness) directions, respectively. The following major observations can be made from these results. The location of the maximum longitudinal and transverse (tensile) residual stresses are near the top of the deposit. For example, after the deposition of the 2nd layer the maximum stress accumulation is observed near the 2nd layer. However, this stress is relieved partially because of the reheating and cooling effects while depositing the upper layers. Therefore, after the deposition

of the 4th layer the maximum stress accumulates near layer 4. Similar observations can be made after the depositions of 6th, 8th and 10th layers. Secondly, in both Figs. 8 and 9, the residual stresses change from tensile to compressive at the interfaces of the two successive layers as indicated in the figures. Finally, the through-thickness stress in Fig. 10 is compressive in the center of the deposit and tensile near the start and stop at the substrate deposit interface. These computed stress results can be useful in the future to study the delamination of deposit from substrate, separation of layers and warping.

Fig. 11 shows a fair agreement between the calculated residual stresses with the corresponding experimentally measured values [37] for a dissimilar metal deposition of IN 718 on a Ti-6Al-4V substrate. Fig. 11(a) and (b) represents the longitudinal and through-thickness components of the residual stresses, respectively. The stresses were measured at different locations along path 1 marked in Fig. 1. Several measurements were taken at the same location to estimate the error bar [37]. The reasons for the slight mismatch between the experimental and calculated values could be caused by the measurement difficulty and the assumptions used in numerical calculations; both are susceptible to some errors.

To understand the effect of alloy on the residual stresses, Fig. 12 compares the distribution of the residual stress components along
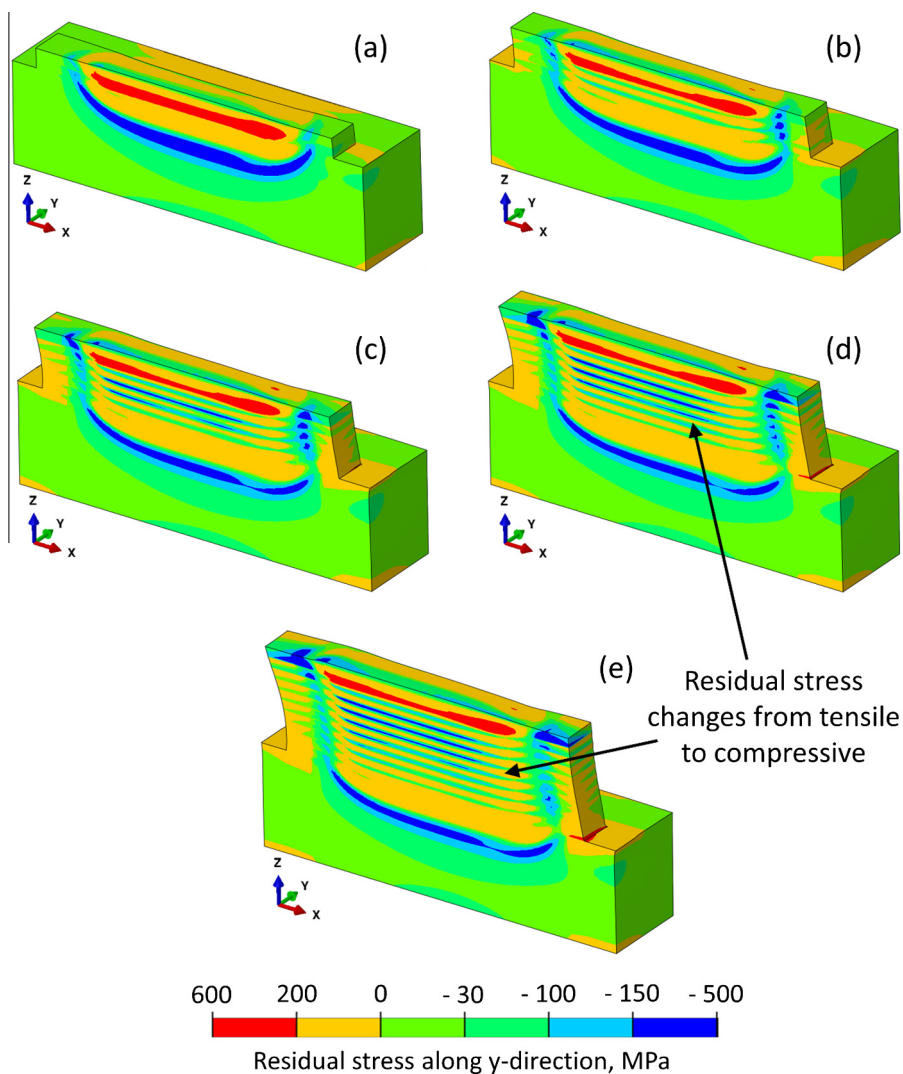
Fig. 9. Residual stress along y-direction (transverse) at the end of the deposition of (a) 2nd (b) 4th (c) 6th (d) 8th and (e) 10th layer of IN 718 powder on IN 718 substrate. Laser beam scanning direction is along the positive x-axis. This simulation is done for 300 W laser power and 15 mm/s scanning speed for the solution domain in Fig. 1. Deformation is magnified by 10×.

x, y and z directions at the end of the cooling of 2nd layer of IN 718 and Ti-6Al-4V deposits. All three residual stress components are highly non-uniform, as expected. The residual stresses in the substrate are mostly compressive. There also exists a sharp gradient of stresses at the substrate-deposit interface. For both alloys the longitudinal stress (x-direction) reaches the maximum at the mid length of the deposit and exhibits a sharp decrease toward both ends (free surfaces). A high gradient in through-thickness residual stress (z-direction) at substrate-deposit interface can potentially cause the separation of the component from the substrate (i.e., delamination). The yield strength of Ti-6Al-4V at room temperature is much higher than that of IN 718 (see Tables 2 and 3). Therefore, the residual stresses are much higher for Ti-6Al-4V as shown in Fig. 12.

Fig. 13(a) also shows that the longitudinal stress along path 1 for Ti-6Al-4V is higher than that for IN 718. However, susceptibility to warping and delamination depends not only on the magnitude of the residual stresses but also the yield strength of the alloy. Therefore, a normalized residual stress [38,39] expressed as the ratio of the longitudinal residual stress along path 1 to the room-temperature yield strength of the alloy is used for assessment of such problems. Fig. 13(b) shows that the normalized stress along

path 1 is higher for IN 718 than that of Ti-6Al-4V. This is because of the lower yield strength of IN 718 than Ti-6Al-4V (Tables 2 and 3). Therefore, under same processing conditions, IN 718 is more susceptible to warping and delamination from the perspective of residual stresses. The high susceptibility to warping and delamination of additively manufactured Inconel 718 components is also reported by Prabhakar et al. [40]. It should also be mentioned that the through-thickness stress along path 2 is always lower than the yield strength of the alloy. For example, under the same conditions of Fig. 13, the maximum through-thickness stresses for IN 718 and Ti-6Al-4V are 100 MPa and 450 MPa, respectively.

The formation of tensile residual stresses has significant effects on the mechanical properties of the product. For example, Fig. 14, a plot based on independent literature data [41,42], shows that the fatigue cracks in additively manufactured Ti-6Al-4V parts grow faster in the presence of a higher tensile residual stress in the component. The maximum tensile residual stress values are estimated from the reported stress distributions [41,42]. The y-intercept of the curve is about 8×10^{-6} mm/cycle which corresponds to the crack growth rate with very low residual stresses (such as the traditionally processed Ti-6Al-4V parts) [43]. In the subsequent para-

500   100   0   - 100   - 200   - 300
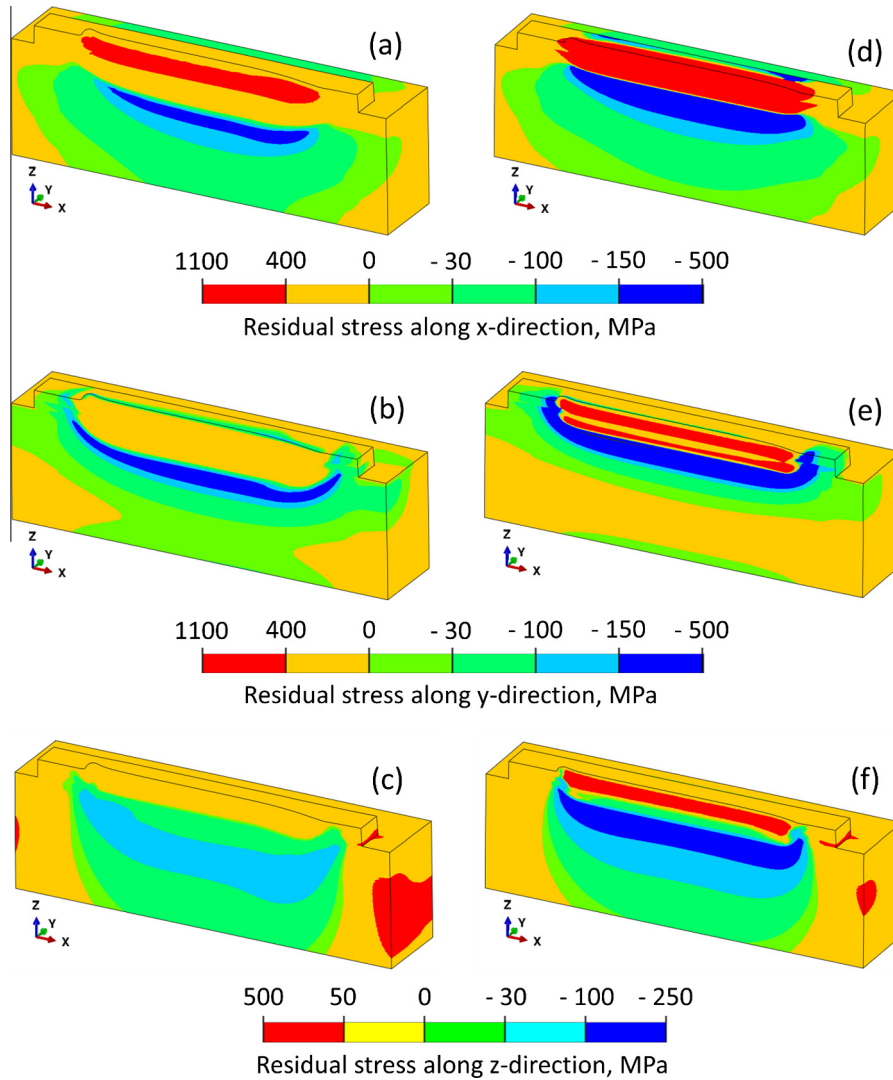
Residual stress along z-direction, MPa
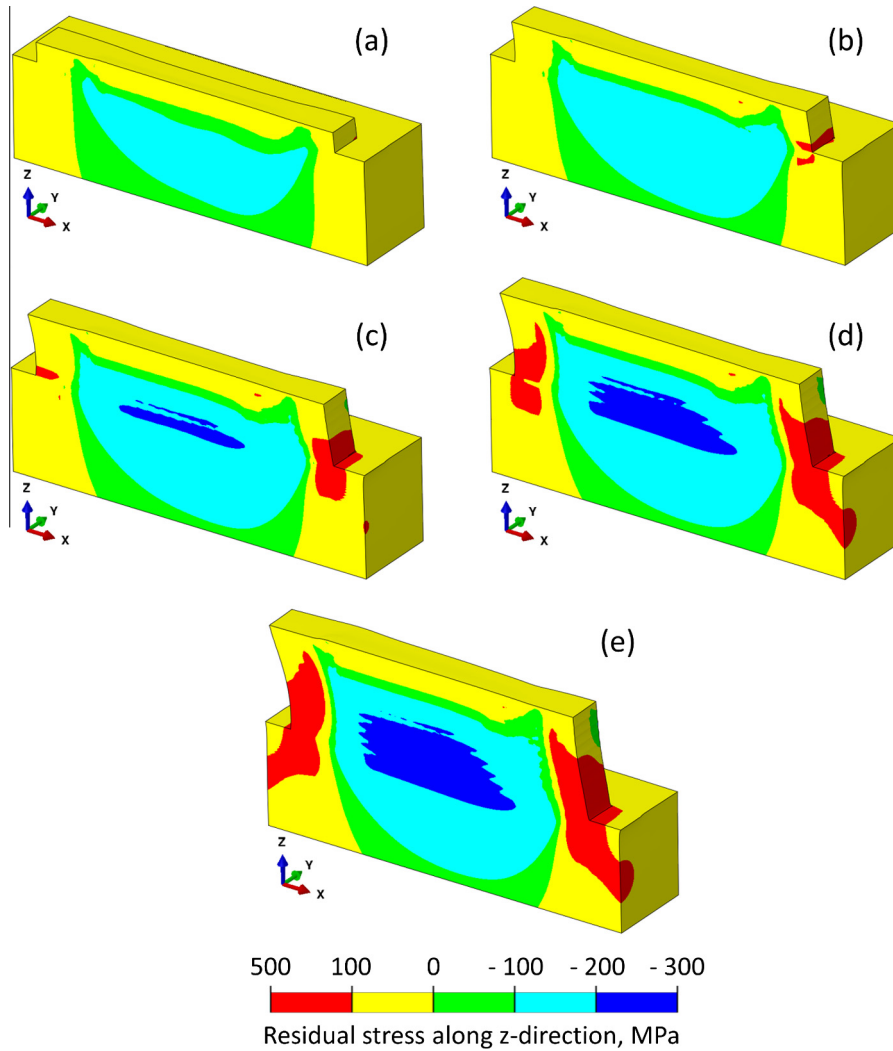
Fig. 10. Residual stress along z-direction (through-thickness) at the end of the deposition of (a) 2nd (b) 4th (c) 6th (d) 8th and (e) 10th layer of IN 718 powder on IN 718 substrate. Laser beam scanning direction is along the positive x-axis. This simulation is done for 300 W laser power and 15 mm/s scanning speed for the solution domain in Fig. 1. Deformation is magnified by 10×.
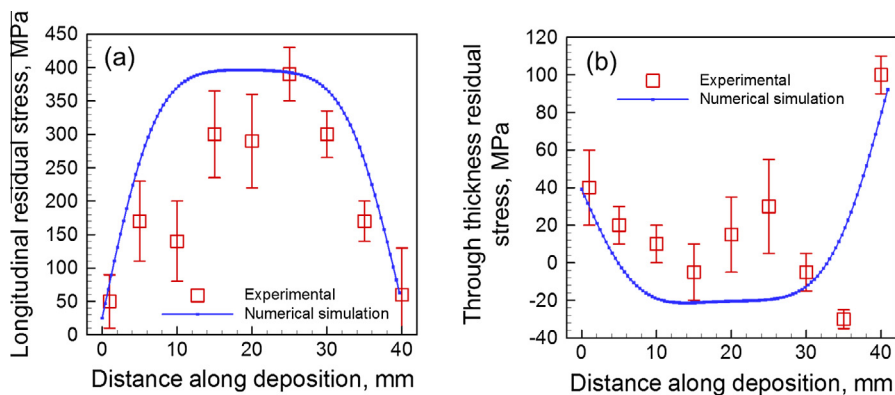

Fig. 11. Comparison of experimentally measured [37] and numerically computed (a) longitudinal residual stress and (b) through-thickness residual stress during the laser deposition of IN 718 powder on a Ti-6Al-4V substrate using process parameter set 2 in Table 5.

graphs the residual stresses resulting from different layer thickness and heat input are discussed to provide a preliminary assessment on the effect of processing parameters on the mechanical property of additively manufactured parts.

Fig. 15(a) and (b) shows the longitudinal and through-thickness residual stress distributions, respectively, during the deposition of a 0.8-mm-high wall using 2 and 4 layers. Building the same height using more layers requires a lower layer thickness. For the same

Fig. 12. Residual stress distribution for IN 718 along (a) x (b) y and (c) z directions, and for Ti-6Al-4V along (d) x (e) y and (f) z directions of the 2 layers deposit. Laser beam scanning direction is along the positive x-axis. The simulations are done for 250 W laser power and 15 mm/s scanning speed for the solution domain in Fig. 1.
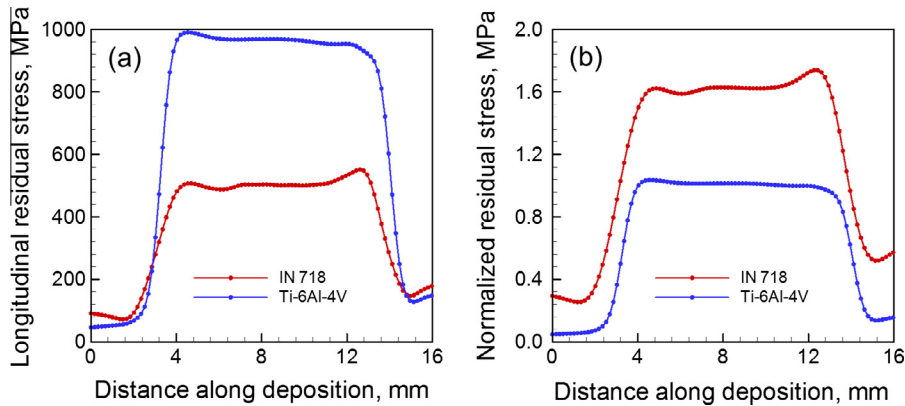
Fig. 13. (a) The longitudinal and (b) the normalized residual stress (longitudinal residual stress/yield strength) distributions along path 1 for IN 718 and Ti-6Al-4V for 250 W laser power and 15 mm/s scanning speed.

laser power and scanning speed, a lower layer thickness increases the volumetric heat flux intensity and hence the peak temperature. At the same time, it takes longer time to build the same height using thinner layers. Therefore, the total deposition time increases. Both the higher peak temperature and more exposure time tend to

increase the distortion [44]. However, the deformation can reduce the residual stresses in the deposit. Therefore, both the longitudinal and the through-thickness residual stresses decrease with an increasing number of layers as shown in Fig. 15. For the deposition conditions studied here, the maximum longitudinal and through-
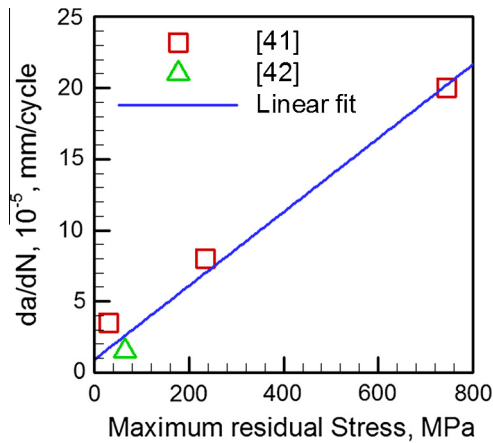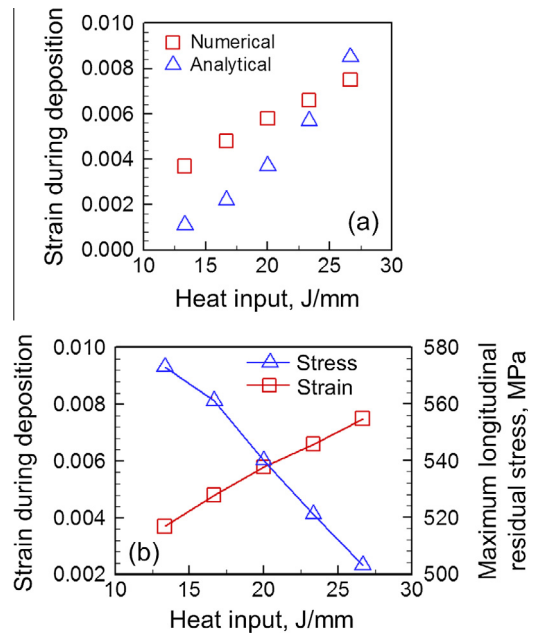
Fig. 14. Fatigue crack growth rate (da/dN) for additively manufactured Ti-6Al-4V components as a function of maximum tensile residual stress. The data are obtained from the crack growth rate curves reported in independent literature studies [41,42]. The stress intensity factor ratio is 0.1 and the stress intensity factor range is 10 MPa m$^{1/2}$.

Fig. 16. (a) Variation of thermal strain during deposition as a function of heat input calculated both numerically and analytically, and (b) effect of heat input on maximum longitudinal stress and strain. Both the plots are drawn for 2 layers of IN 718 deposit on IN 718 substrate.

thickness residual stresses can be reduced by about 20% and 30%, respectively by using 4 layers to build the same height instead of 2 layers, as shown in Fig. 15.

To understand the effect of heat input and peak temperature on the distortion and strain, we have recently proposed [44] a strain parameter (ε^*) as an indicator of the susceptibility to distortion.

$$\varepsilon^* = \frac{\beta \Delta T}{EI} \frac{tH^{3/2}}{F_o \sqrt{\rho}} \qquad (10)$$

where β is the volumetric coefficient of thermal expansion, ΔT is the maximum rise in temperature during the process, E is the elastic modulus, I is the moment of inertia of the substrate, t is the characteristic time, H is the heat input per unit length, F_o is the Fourier number, and ρ is the density of the alloy. The product, EI, is the flexural rigidity of the structure. Fourier number is the ratio of the heat storage rate to heat dissipation rate. The temperature rise and the Fourier number are both calculated using the heat transfer and fluid flow model. This strain parameter quantitatively represents the peak thermal strain encountered by the fabricated part [44]. Higher heat input increases the peak temperature as well as the pool volume [45]. Larger pools shrink more during solidification and exhibit more distortion. Therefore, strains increase with the heat input. Fig. 16(a) compares the peak thermal strains at the end of the deposition calculated both numerically using the thermo-mechanical model as well as analytically using Eq. (10). Eq. (10)

does not consider the plastic strain, and this is probably the reason for the slight mismatch between the analytical and numerical results in Fig. 16(a).

Fig. 16(b) shows that doubling the heat input increases the strain by almost 2.5 times. However, the maximum longitudinal residual stresses can be reduced by about 20% by doubling the heat input. Distortion is often a crucial issue in AM as it affects the dimensional accuracy of the fabricated part [44,46]. On the other hand, the residual stresses can be reduced by post process heat treatment or by reducing the layer thickness. Therefore, an appropriate processing condition is to be carefully selected considering both the distortion and residual stresses. In Fig. 16(b), for example, a heat input of 20 J/mm seems to provide a strain of 0.0057 and a longitudinal residual stress of 540 MPa. This figure is useful to select a heat input considering both the maximum longitudinal residual stress and strain. In practice lower heat input can be achieved by low laser power and faster scanning speed. The layer thickness may also be kept low in order to minimize the residual stresses. This finding is consistent with the current industrial practice. For example, General Electric uses low heat input (100–500 W and 2000 mm/s) and low layer thickness of 40–100 μm to fabricate
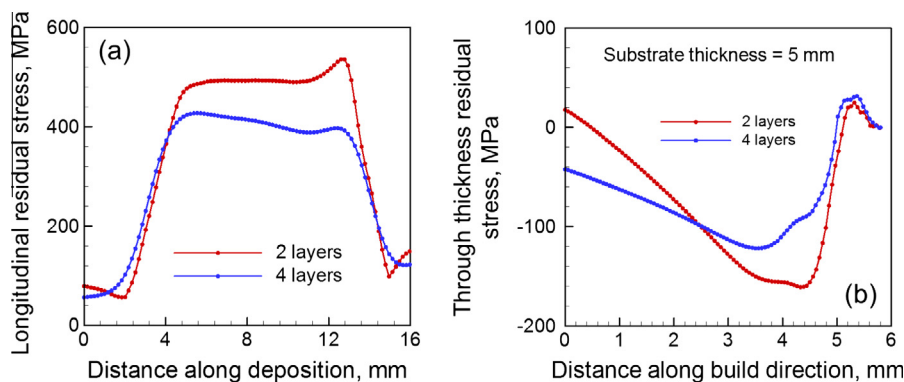
Fig. 15. (a) The longitudinal and (b) the through-thickness residual stress distributions of IN 718 deposit on IN 718 substrate for the process parameter set 3 in Table 5 using 2 and 4 layers deposition to build a 0.8-mm-high wall. The simulations are done for 250 W laser power and 15 mm/s scanning speed.

aero-engine fuel nozzles [47]. Such improved predictive models are essential to help select process parameters and evaluate other strategies such as preheating for mitigating residual stresses and distortion in the future.

4. Summary and conclusions

The evolution of the stresses and strains for Inconel 718 and Ti-6Al-4V and their dependence on important process parameters such as heat input and layer thickness are investigated using a coupled thermal, fluid flow and mechanical model. This model is used to estimate the appropriate heat input and layer thickness to fabricate dimensionally accurate components with low residual stresses. Below are the specific findings.

(1) Ti-6Al-4V components suffer higher residual stresses than IN 718 under the same processing conditions. However, IN 718 parts are more susceptible to warping, delamination and buckling because of their higher residual stress to yield strength ratio.
(2) The AM parts fabricated using thin layers encounter a high peak temperature and long exposure time under the laser beam. As a result, the residual stresses can be decreased as much as 30% by reducing the thickness of each layer to fabricate the component. This finding is consistent with the industrial practice of 40–100 μm layer thickness to produce aero engine fuel nozzles.
(3) Doubling the heat input can reduce the residual stresses by about 20%. However, the same condition enhances the thermal distortion by about 2.5 times. Therefore, an appropriate heat input selected by trading off both distortion and residual stresses will be helpful to fabricate a dimensionally accurate part with good mechanical properties.
(4) The longitudinal residual stress exhibits a steep gradient at the both ends of the deposit that makes the parts susceptible to buckling and warping. The through-thickness stress that is responsible for the possible delamination of a component changes sharply at the substrate deposit interface. The residual stress changes from tensile to compressive at the layer interfaces. In extreme cases, this behavior may result in the separation of layers.

It is hoped that the procedure proposed here will constitute a step forward in predictive modeling and results will be useful to assess residual stresses and make dimensionally compliant AM components.

Acknowledgement

References

[1] D.D. Gu, W. Meiners, K. Wissenbach, R. Poprawe, Laser additive manufacturing of metallic components: materials, processes and mechanisms, Int. Mater. Rev. 57 (2012) 133–164.
[2] W.J. Sames, F.A. List, S. Pannala, R.R. Dehoff, S.S. Babu, The metallurgy and processing science of metal additive manufacturing, Int. Mater. Rev. (2016) 1–46.
[3] J. Ding, P. Colegrove, J. Mehnen, S. Ganguly, P.M. Sequeira Almeida, F. Wang, S. Williams, Thermo-mechanical analysis of wire and arc additive layer manufacturing process on large multi-layer parts, Comput. Mater. Sci. 50 (2011) 3315–3322.
[4] P.H. Chang, T.L. Teng, Numerical and experimental investigations on the residual stresses of the butt-welded joints, Comput. Mater. Sci. 29 (2004) 511–522.
[5] D. Deng, H. Murakawa, Numerical simulation of temperature field and residual stress in multi-pass welds in stainless steel pipe and comparison with experimental measurements, Comput. Mater. Sci. 37 (2006) 269–277.
[6] R.J. Moat, A.J. Pinkerton, L. Li, P.J. Withers, M. Preuss, Residual stresses in laser direct metal deposited Waspaloy, Mater. Sci. Eng. A 528 (2011) 2288–2298.
[7] P. Rangaswamy, M.L. Griffith, M.B. Prime, T.M. Holden, R.B. Rogge, J.M. Edwards, R.J. Sebring, Residual stresses in LENS® components using neutron diffraction and contour method, Mater. Sci. Eng. A 399 (2005) 72–83.
[8] G. Bussu, P.E. Irving, The role of residual stress and heat affected zone properties on fatigue crack propagation in friction stir welded 2024-T351 aluminum joints, Int. J. Fatigue 25 (2003) 77–88.
[9] A.S. Wu, D.W. Brown, M. Kumar, G.F. Gallegos, W.E. King, An experimental investigation into additive manufacturing-induced residual stresses in 316L stainless steel, Metal. Mater. Trans. A 45 (2014) 6260–6270.
[10] J. Zhang, X. Wang, S. Paddea, X. Zhang, Fatigue crack propagation behaviour in wire + arc additive manufactured Ti-6Al-4V: effects of microstructure and residual stress, Mater. Des. 90 (2016) 551–561.
[11] A. Riemer, S. Leuders, M. Thöne, H.A. Richard, T. Tröster, T. Niendorf, On the fatigue crack growth behavior in 316L stainless steel manufactured by selective laser melting, Eng. Fract. Mech. 120 (2014) 15–25.
[12] L.M. Sochalski-Kolbus, E.A. Payzant, P.A. Cornwell, T.R. Watkins, S.S. Babu, R.R. Dehoff, M. Lorenz, O. Ovchinnikova, C. Duty, Comparison of residual stresses in Inconel 718 simple parts made by electron beam melting and direct laser metal sintering, Metal. Mater. Trans. A 46 (2015) 1419–1432.
[13] D. Qiao, W. Zhang, T.-Y. Pan, P. Crooker, S. David, Z. Feng, Evaluation of residual plastic strain distribution in dissimilar metal weld by hardness mapping, Sci. Technol. Weld. Join. 18 (2013) 624–630.
[14] P.J. Withers, H.K.D.H. Bhadeshia, Residual stress. Part 1 – measurement techniques, Mater. Sci. Technol. 17 (2001) 355–365.
[15] G.S. Schajer, Application of finite element calculations to residual stress measurements, J. Eng. Mater. Technol. 103 (1981) 157–163.
[16] V. Manvatkar, A. De, T. DebRoy, Heat transfer and material flow during laser assisted multi-layer additive manufacturing, J. Appl. Phys. 116 (2014) 124905.
[17] V. Manvatkar, A. De, T. DebRoy, Spatial variation of melt pool geometry, peak temperature and solidification parameters during laser assisted additive manufacturing process, Mater. Sci. Technol. 31 (2015) 924–930.
[18] S.A. David, T. DebRoy, Current issues and problems in welding science, Science 257 (1992) 497–502.
[19] A. Raghavan, H.L. Wei, T.A. Palmer, T. DebRoy, Heat transfer and fluid flow in additive manufacturing, J. Laser Appl. 25 (2013) 052006.
[20] A. Vasinonta, J.L. Beuth, M. Griffith, Process maps for predicting residual stress and melt pool size in the laser-based fabrication of thin-walled structures, J. Manuf. Sci. Eng. 129 (2007) 101–109.
[21] M.P. Mughal, H. Fawad, R.A. Mufti, M. Siddique, Deformation modelling in layered manufacturing of metallic parts using gas metal arc welding: effect of process parameters, Model. Simul. Mater. Sci. Eng. 13 (2005) 1187.
[22] A.H. Nickel, D.M. Barnett, F.B. Prinz, Thermal stresses and deposition patterns in layered manufacturing, Mater. Sci. Eng. A 317 (2001) 59–64.
[23] S. Ghosh, J. Choi, Three-dimensional transient finite element analysis for residual stresses in the laser aided direct metal/material deposition process, J. Laser Appl. 17 (2005) 144–158.
[24] P. Mercelis, J.P. Kruth, Residual stresses in selective laser sintering and selective laser melting, Rapid Prototyp. J. 12 (2006) 254–265.
[25] L. Wang, S.D. Felicelli, P. Pratt, Residual stresses in LENS-deposited AISI 410 stainless steel plates, Mater. Sci. Eng. A 496 (2008) 234–241.
[26] G. Vastola, G. Zhang, Q.X. Pei, Y-W. Zhang, Controlling of residual stress in additive manufacturing of Ti6Al4V by finite element modeling, Addit. Manuf. (2016), http://dx.doi.org/10.1016/j.addma.2016.05.010.
[27] Z. Nie, G. Wang, J.D. McGuffin-Cawley, B. Narayanan, S. Zhang, D. Schwam, M. Kottman, Y.K. Rong, Experimental study and modeling of H13 steel deposition using laser hot-wire additive manufacturing, J. Mater. Process. Technol. 235 (2016) 171–186.
[28] M. Alimardani, E. Toyserkani, J.P. Huissoon, A 3D dynamic numerical approach for temperature and thermal stress distributions in multilayer laser solid freeform fabrication process, Opt. Laser Eng. 45 (2007) 1115–1130.
[29] L.E. Svensson, B. Gretoft, H.K.D.H. Bhadeshia, An analysis of cooling curves from the fusion zone of steel weld deposits, Scand. J. Metall. 15 (1986) 97–103.
[30] K.C. Mills, Recommended Values of Thermo-Physical Properties for Selected Commercial Alloys, Woodhead Publishing, Cambridge, 2002.
[31] Abaqus Documentation, Version 6.14, Dassault Systems, 2015.
[32] A. Kamara, S. Marimuthu, L. Li, A numerical investigation into residual stress characteristics in laser deposited multiple layer waspaloy parts, Trans. ASME-B – J. Manuf. Sci. Eng. 133 (2011) 1–9.
[33] P. Scott, R. Olson, J. Bockbrader, M. Wilson, B. Gruen, R. Morbitzer, Y. Yang, C. Williams, F. Brust, L. Fredette, N. Ghadiali Battelle, The Battelle Integrity of Nuclear Piping (BINP), Program Final Report, Columbus, OH, 2005.
[34] T. Seshacharyulu, S.C. Medeiros, W.G. Frazier, Y.V.R.K. Prasad, Microstructural mechanisms during hot working of commercial grade Ti–6Al–4V with lamellar starting structure, Mater. Sci. Eng. A 325 (2002) 112–125.
[35] P. Rangaswamy, H. Choo, M.B. Prime, M.A. Bourke, J.M. Larsen, High temperature stress assessment in SCS-6/Ti-6Al-4V composite using neutron diffraction and finite element modeling, in: International Conference on Processing & Manufacturing of Advanced Materials, Las Vegas, NV, USA, 2000.

[36] F. Lia, R.M. Martukanitz, J.Z. Park, T. DebRoy, T. Mukherjee, J.S. Keist, S.N. Patankar, Process and microstructural validation of the laser-based directed energy deposition process for Ti-6Al-4V and Inconel 625 material, Mater. Sci. Technol. (2015) (Columbus, OH, USA), The abstract can be retrieved from: <http://www.programmaster.org/PM/PM.nsf/ApprovedAbstracts/A0DC8061FC54E5B785257E0A0073048E?OpenDocument>.

[37] K. Shah, I.U. Haq, S.A. Shah, F.U. Khan, M.T. Khan, S. Khan, Experimental study of direct laser deposition of Ti-6Al-4V and Inconel 718 by using pulsed parameters, Sci. World J. 2014 (2014).

[38] A.M. Al-Mukhtar, Residual stresses and stress intensity factor calculations in T-welded joints, J. Fail. Anal. Prevent. 13 (2013) 619–623.

[39] R. Jackson, I. Chusoipin, I. Green, A finite element study of the residual stress and deformation in hemispherical contacts, J. Tribol. 127 (2005) 484–493.

[40] P. Prabhakar, W.J. Sames, R. Dehoff, S.S. Babu, Computational modeling of residual stress formation during the electron beam melting process for Inconel 718, Addit. Manuf. 7 (2015) 83–91.

[41] S. Leuders, M. Thöne, A. Riemer, T. Niendorf, T. Tröster, H.A. Richard, H.J. Maier, On the mechanical behaviour of titanium alloy TiAl6V4 manufactured by selective laser melting: fatigue resistance and crack growth performance, Int. J. Fatigue 48 (2013) 300–307.

[42] P. Edwards, A. O'Conner, M. Ramulu, Electron beam additive manufacturing of titanium components: properties and performance, J. Manuf. Sci. Eng. 135 (2013) 061016.

[43] A.G. Gavras, F.C. Brendan, D.A. Lados, Effects of microstructure on the fatigue crack growth behavior of light metals and design considerations, Matéria (Rio de Janeiro) 15 (2010) 319–329.

[44] T. Mukherjee, J.S. Zuback, A. De, T. DebRoy, Printability of alloys for additive manufacturing, Sci. Rep. 6 (2016).

[45] H.L. Wei, J.W. Elmer, T. DebRoy, Origin of grain orientation during solidification of an aluminum alloy, Acta Mater. 115 (2016) 123–131.

[46] T. Mukherjee, V. Manvatkar, A. De, T. DebRoy, Mitigation of thermal distortion during additive manufacturing, Scripta Mater. 127 (2017) 79–83.

[47] P.M. Kenney, D.E. Lindley, General Electric Company, 2013, U.S. Patent Application 14/440, 154.